SUPPLEMENTARY INFORMATION

Surfactant-templated syntheses of nanostructured high-entropy spinel oxide electrocatalyst and effects on water-splitting

Jimodo J. Ogada[1], Augustus K. Lebechi[1], Aderemi Haruna[1], and Kenneth I. Ozoemena[1]*

[1]*School of Chemistry, University of the Witwatersrand, Braamfontein, 2050, Johannesburg, South Africa*

Table of Contents

Table of Figures

Table of Schemes

List of Tables

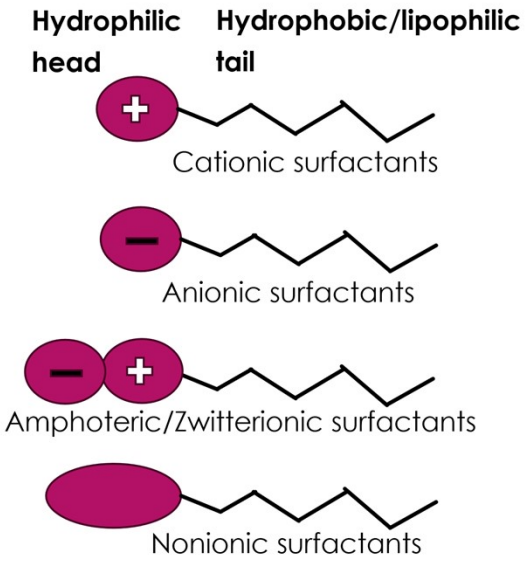

Scheme S 1: A schematic representation of the different types of surfactants

Materials

Cobalt (II) nitrate hexahydrate (Cobaltous nitrate, $Co(NO_3)_2 \cdot 6H_2O$, Sigma Aldrich, Assay: ≥99.99% trace metals basis), Copper(II) nitrate trihydrate ($Cu(NO_3)_2 \cdot 3H_2O$, Sigma Aldrich, Assay: ≥99.99% trace metals basis), Ferric nitrate nonahydrate ($Fe(NO_3)_3 \cdot 9H_2O$, Sigma Aldrich, Assay: ≥99.95% trace metals basis), Manganese Nitrate Tetrahydrate ($Mn(NO_3)_2.4H_2O$, Sigma Aldrich, Assay: ≥99.9% trace metals basis), Nickel(II) nitrate hexahydrate ($Ni(NO_3)_2.6H_2O$, Sigma Aldrich, Assay: ≥99.999% trace metals basis), 25% ammonia solution (NH_4OH), Polyvinylpyrrolidone (PVP, 360kDa, Sigma Aldrich), Hexadecyltrimethylammonium bromide (CTAB, Sigma Aldrich), Sodium dodecyl sulfate (SDS, Sigma Aldrich),

All chemicals were used as received without further purification. The deionized water was produced by an ultrapure water system.

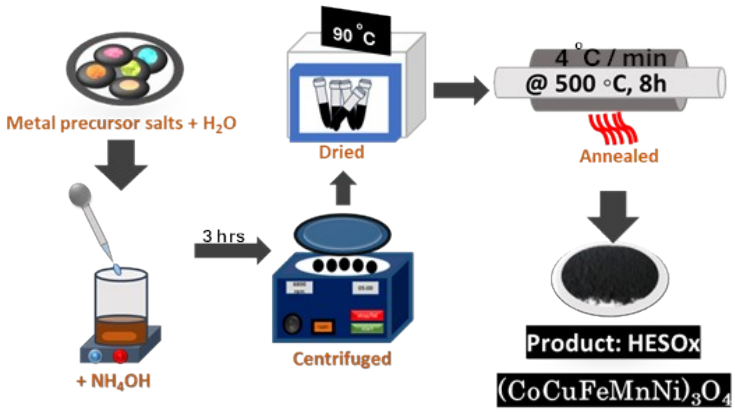

Scheme S 2: Procedures for the synthesis of $(CoCuFeMnNi)_3O_4$

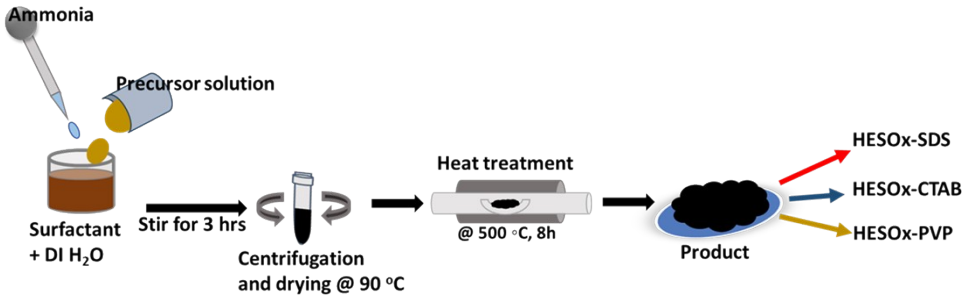

Scheme S 3: Procedures for the surfactant-assisted synthesis of $(CoCuFeMnNi)_3O_4$

Characterizations and Electrochemical Techniques

To understand the crystal structure and phase identification of the synthesized high entropy materials, powder XRD measurements were taken at Bragg's angles between 10 and 90 2θ° at 3.6 2θ°/min using the Bruker D2 Phaser x-ray diffractometer equipped with a Cu Kα source (λ = 1.5406 Å). The information on phase composition was supplemented with Raman spectroscopy measurements. The samples were analyzed on the Thermo Scientific Smart Raman DXR2, using a laser wavelength of 532 nm, with 25 µm gratings, and 5 mW power. The thermal stability of each sample was studied using the Perkin Elmer Thermogravimetric analyzer (TGA)/Differential Thermogravimetric analysis (DTGA) 6000 in an inert environment using N_2 gas. Zeiss Crossbeam 540 was operated at 2 kV for imaging and 20 kV for the EDX. The data was acquired using an Oxford Xmax detector with the Aztec software and using a copper reference. The TriStar II Plus instrument was employed for gas sorption analysis (GSA) in N_2. The X-ray photoelectron spectra

(XPS) were obtained on an AXIS SUPRA instrument, and the deconvolution of the peaks was done using XPSPeak41 software.

All electrochemical measurements were performed on the BioLogic SP300 electrochemical workstation with a typical three-electrode cell as shown in **Scheme S4**. The three-electrode (half-cell) arrangement was constructed with a glassy carbon rotating disk electrode (RDE = 5 mm in diameter) as the working electrode, platinum wire as the counter electrode (to generate applied potentials at the working electrode), and Ag/AgCl (saturated 3 M KCl) as the reference electrode (to monitor the current generated at the working electrode). The RDE was polished on a mirror cloth using alumina (Al_2O_3) slurry (Sigma Aldrich), rinsed with ultrapure water, and allowed to dry.

Each catalyst ink was prepared by dispersing 1 mg of the catalyst powder and 1 mg of onion-like carbon (OLC; Gelon) in 0.5 mL of ethanol and 20 µL of Nafion solution (Sigma Aldrich; 5 wt.% in a mixture of lower aliphatic alcohols and 45% water). Nafion solution was added to the catalyst ink to increase the adherence of the catalyst material to the glassy carbon electrode. The mixture was ultrasonicated for 30 minutes to create a homogeneous ink suspension.

50 µL of the catalyst ink suspension was then deposited in a dropwise fashion on the RDE and left to dry. This preparation produced an electrocatalyst loading of 0.49058 mg/cm^2. All reactions were run in 1.0 M KOH (pH 14) and with Millipore water.

HER and OER polarization curves were obtained using linear sweep voltammetry (LSV) at a scan rate of 10 mV/s. The measured potentials were converted from Ag/AgCl to RHE (reversible hydrogen electrode) by the following equation:

$$E_{RHE} = E^{0}_{Ag/AgCl} + E_{Ag/AgCl} + 0.059pH \quad \text{- - - -} \quad \textbf{Equation 1}$$

Where $E^{0}_{Ag/AgCl}$ is 0.197 V vs RHE, $E_{Ag/AgCl}$ is the measured potential values vs. Ag/AgCl, recorded by the potentiostat.

Information about the charge transfer efficiency was obtained via electrochemical impedance spectroscopy (EIS) in a frequency range of 0.1 Hz to 100 kHz, and the experimental data were fitted using a suitable equivalent circuit.

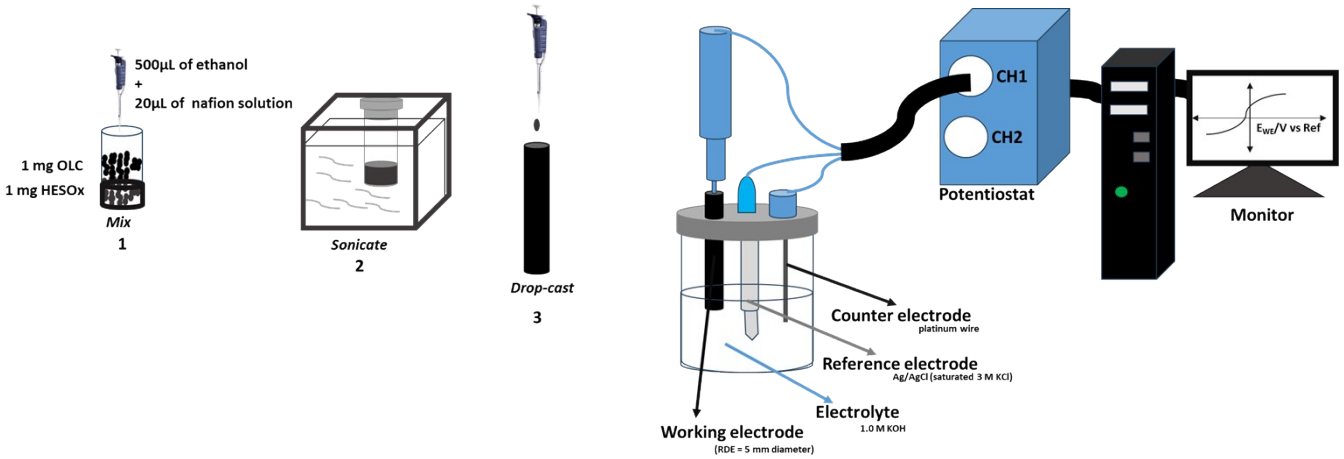

Scheme S 4: Catalyst ink preparation and three-electrode setup

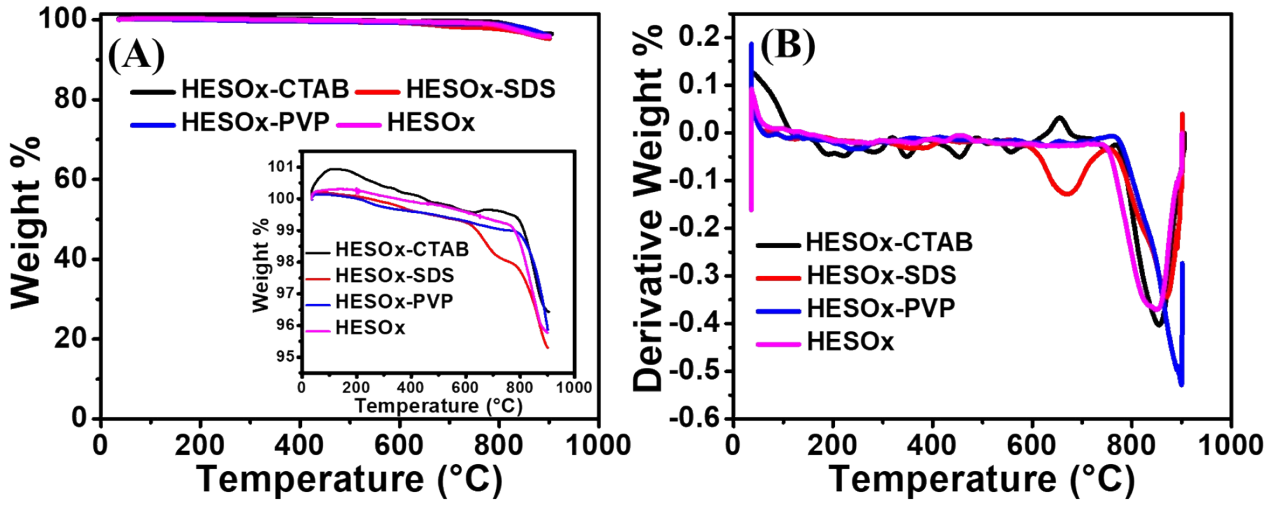

Figure S 1: (A) Thermogravimetric Analysis (TGA) and (B) Derivative Thermogravimetric Analysis (DTGA) of HESOx, HESOx-PVP, HESOx-SDS, and HESOx-CTAB.

At an initial temperature of 32.2 °C, the mass of each sample is seen to slightly increase, exceeding the original mass (100%) before it begins to lose weight. This increase in mass is not reasonable, as the decomposition of the sample always decreases the mass of the sample under investigation. Usually, the initial increase in weight is attributed to the reaction of the sample with the purging gas or absorption of the purging gas. Since nitrogen gas is inert, the increase in weight could be due to the absorption of nitrogen or the buoyancy effect in the TGA equipment, as the sample is measured under some gas atmosphere, exposing it to drag force and buoyancy besides its actual

weight. The buoyancy effect can be removed by running a blank test with the empty TGA pan. Subtracting this blank measurement from the initial TGA measurement results will give the actual mass change.[1]

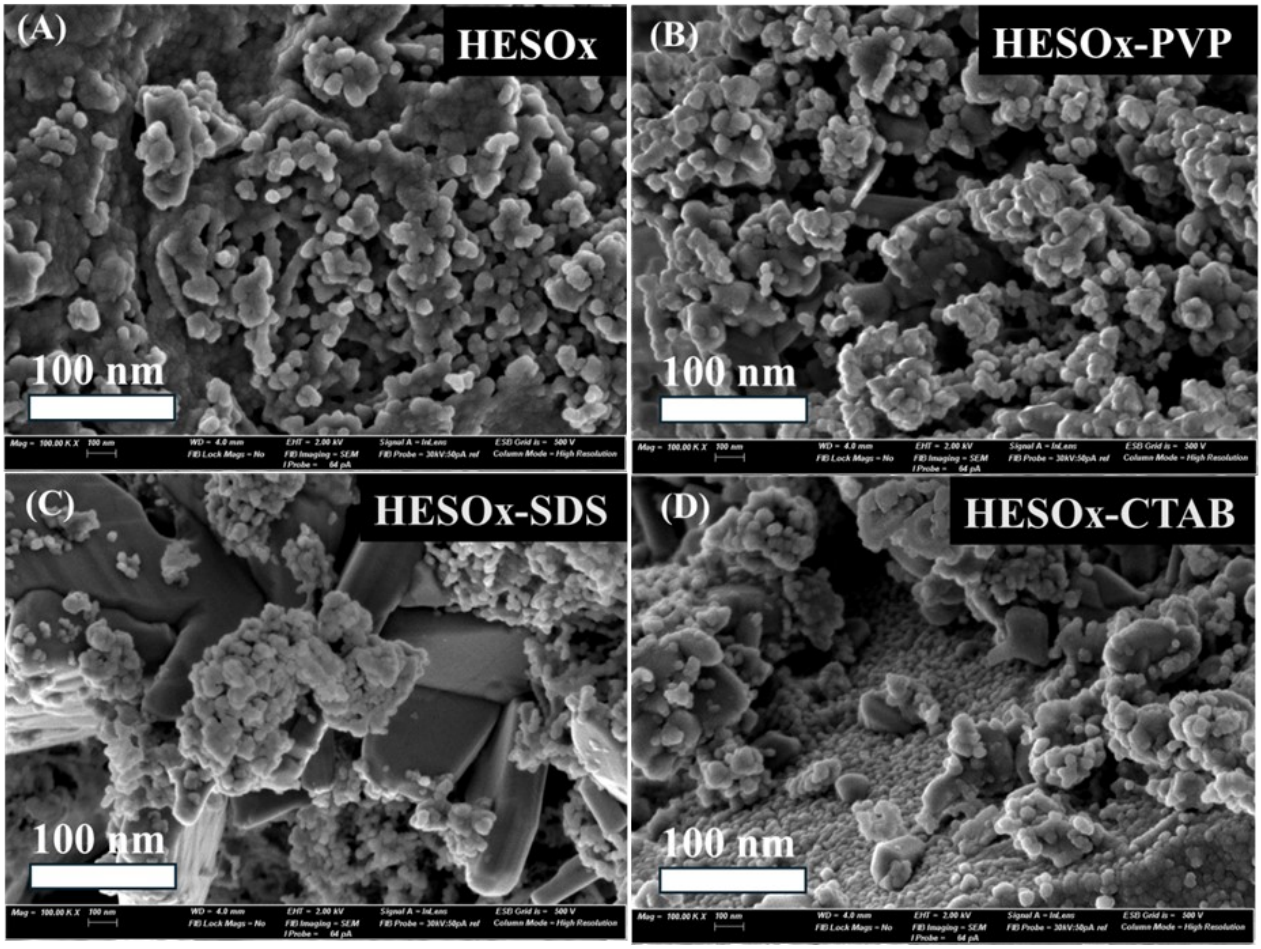

Figure S 2: SEM images of (A) HESOx (B) HESOx-PVP (C) HESOx-SDS (D) HESOx-CTAB

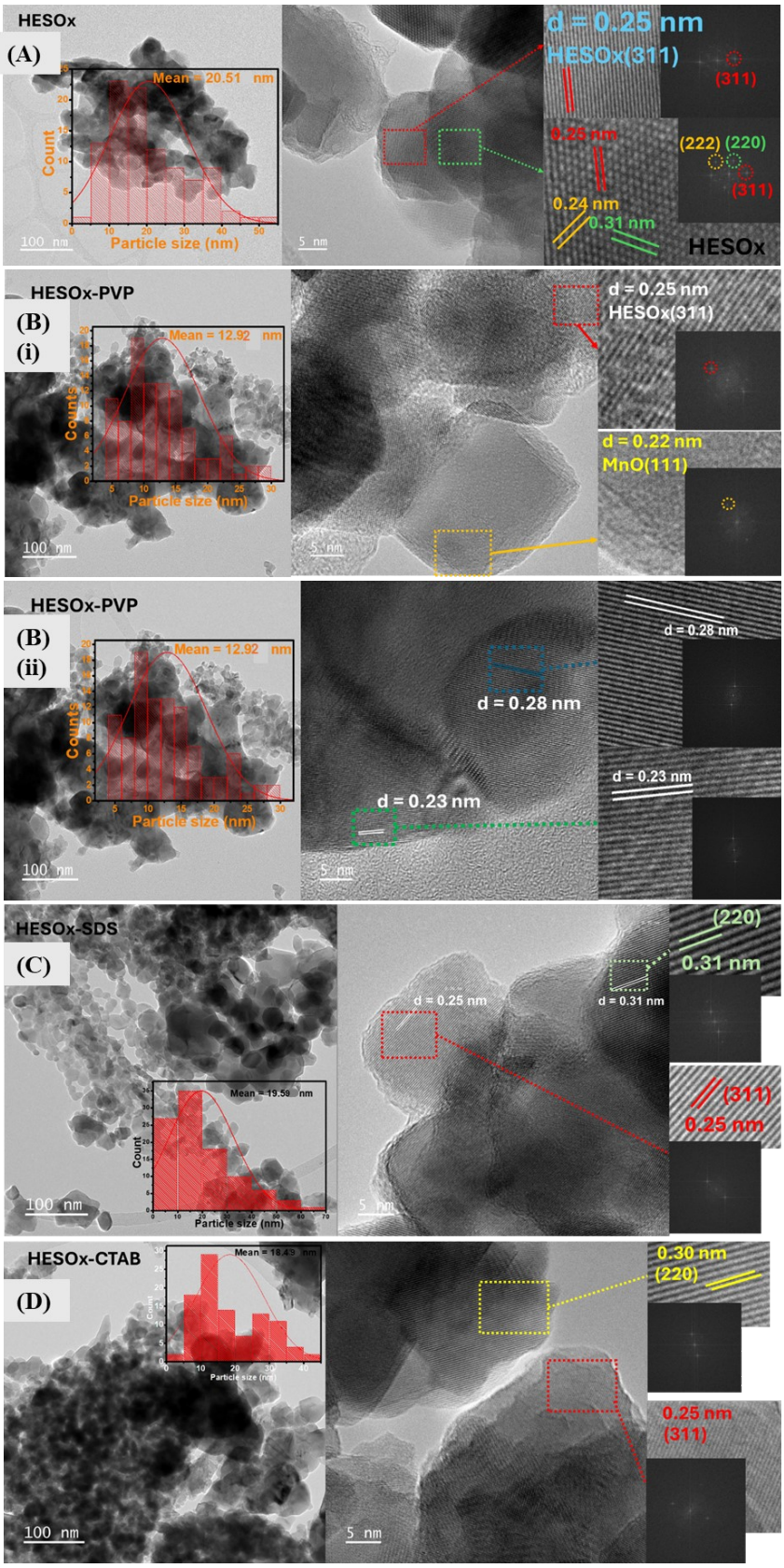

Figure S 3: TEM images and corresponding HRTEM images

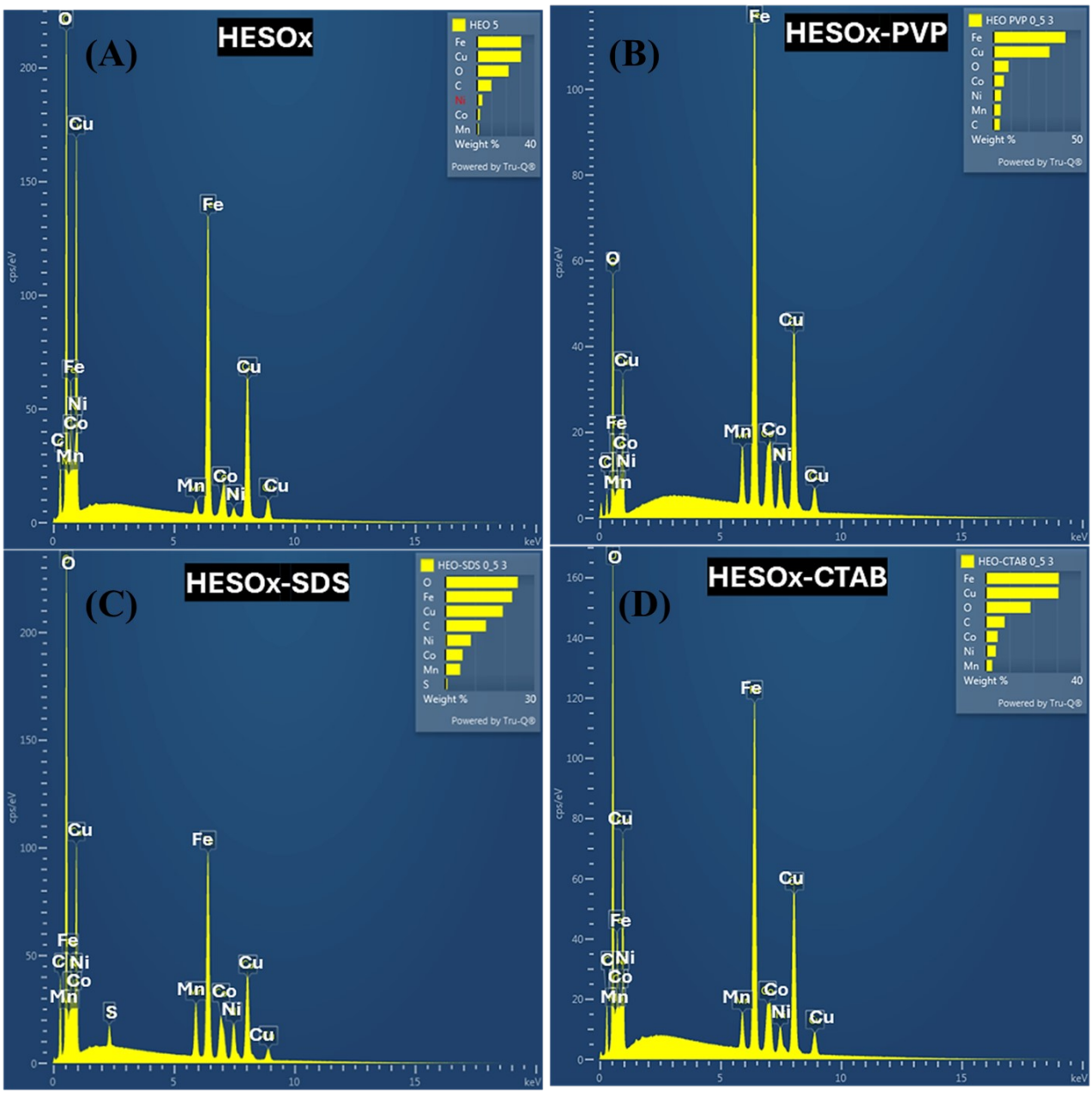

Figure S 4: Elemental Analysis of (A) HESOx (B) HESOx-PVP (C) HESOx-SDS (D) HESOx-CTAB.

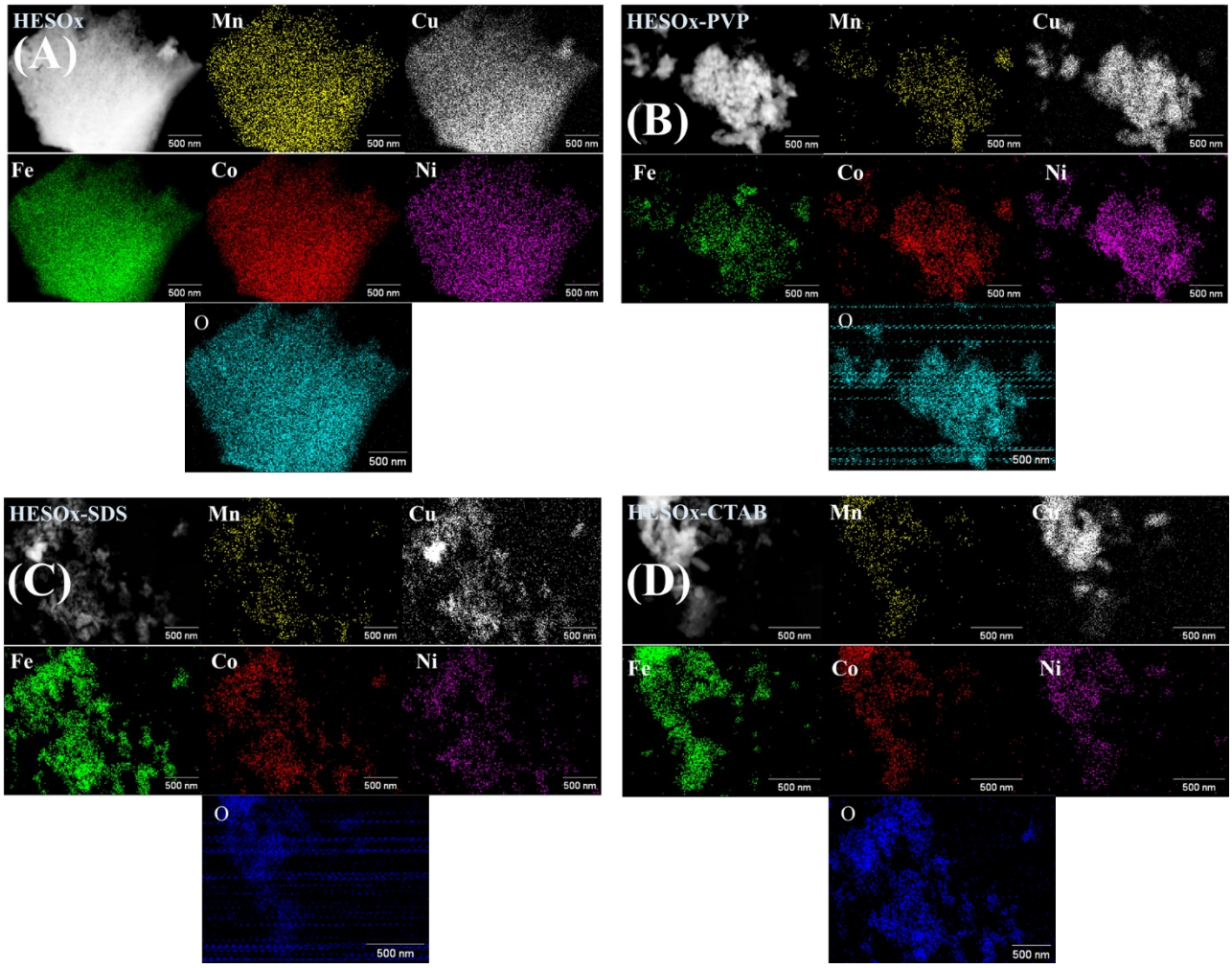

Figure S 5: Elemental mapping of (A) HESOx (B) HESOx-PVP (C) HESOx-SDS (D) HESOx-CTAB

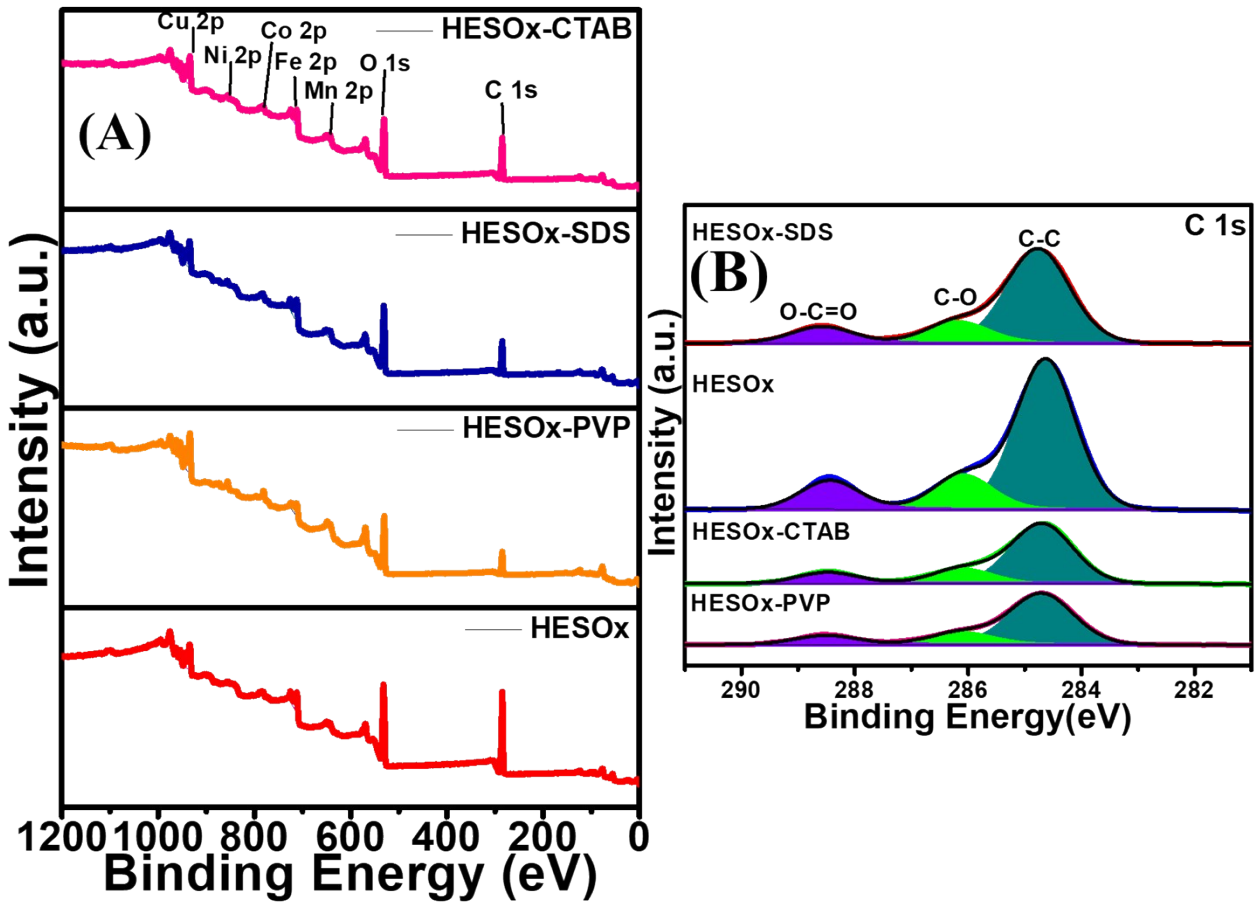

Figure S 6: XPS (A) wide scans and (B) C 1s scans of HESOx, HESOx-PVP, HESOx-SDS, and HESOx-CTAB

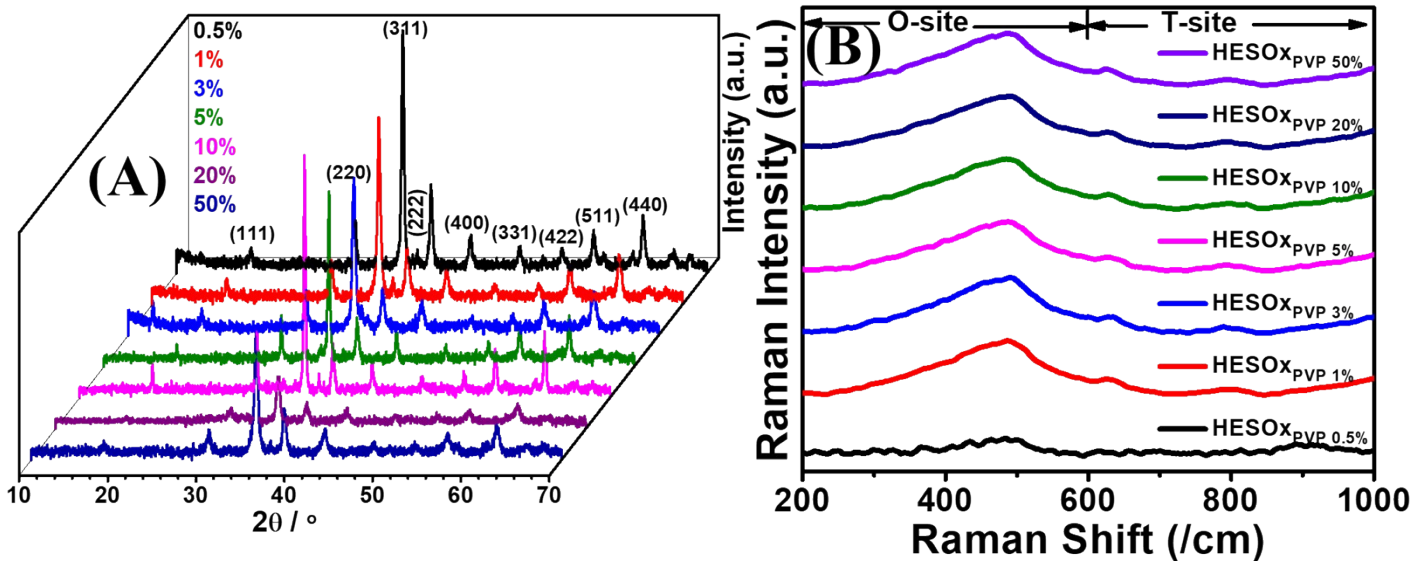

Figure S 7: (A) XRD patterns and (B) Raman spectra of the samples

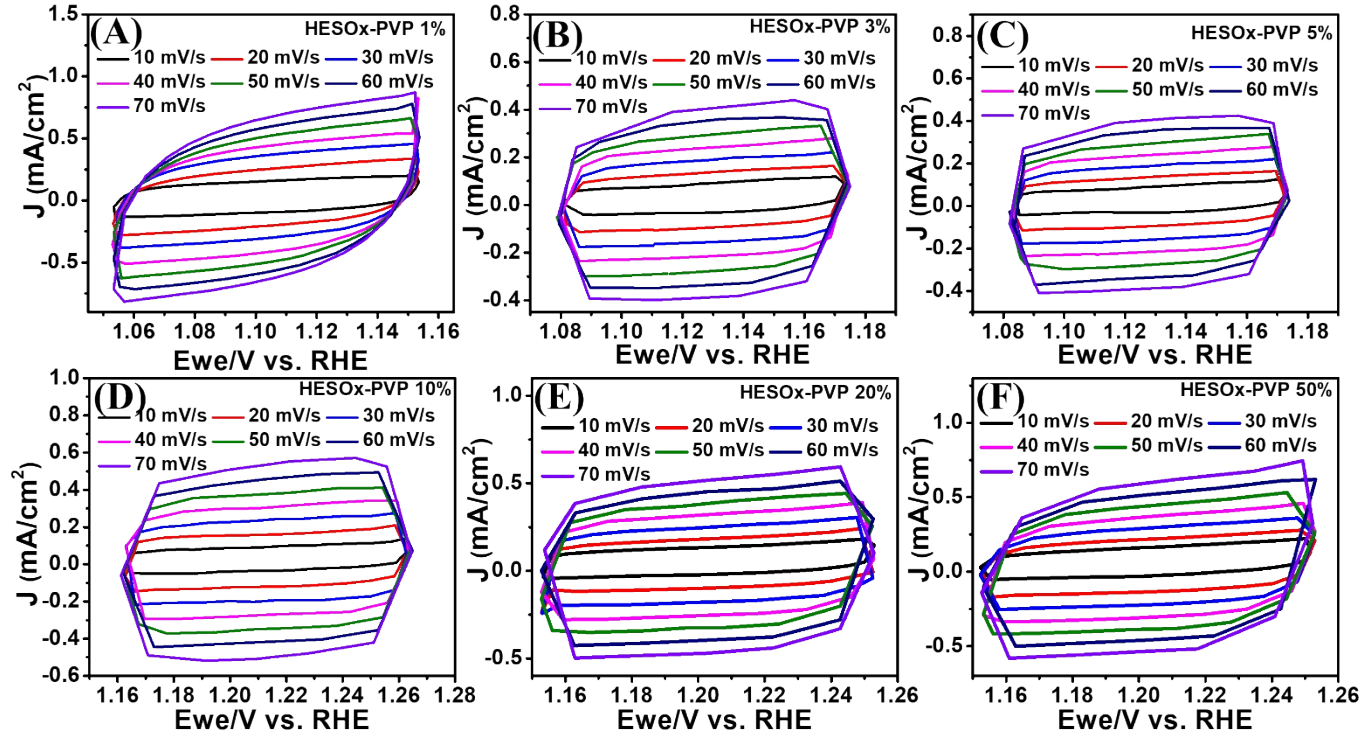

Figure S 8: CV scans of the non-faradaic region of the samples at different scan rates in 1 M KOH

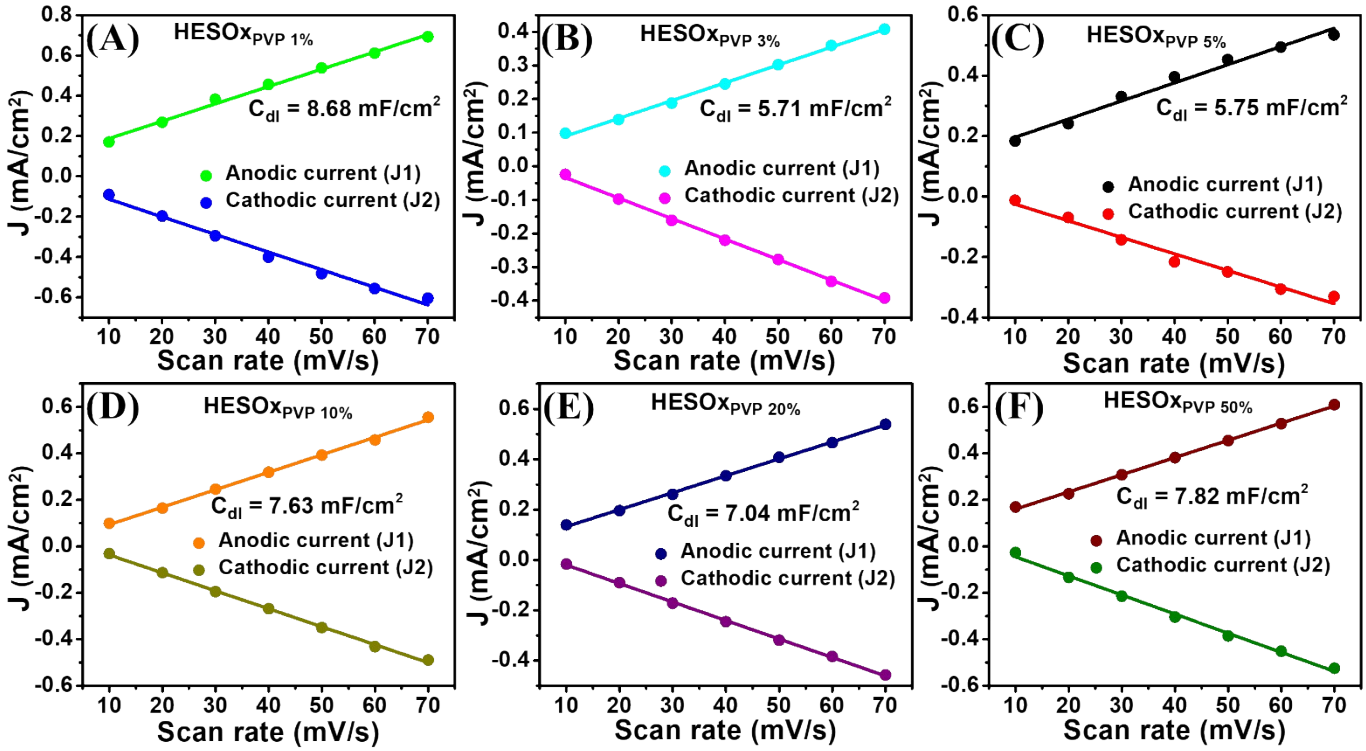

Figure S 9: Linear plots of the non-faradaic anodic and cathodic current density

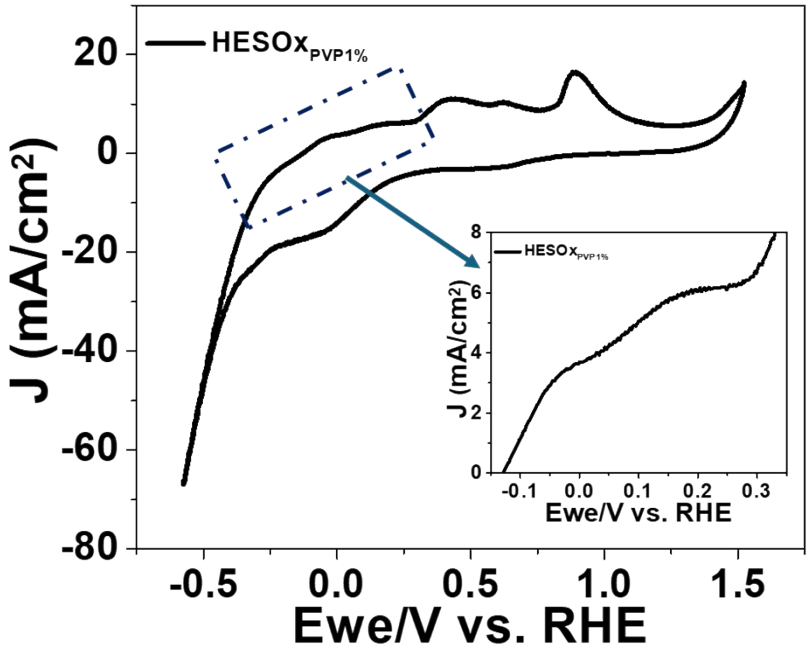

Figure S 10: CV of HESOx$_{PVP\ 1\%}$ at 1600 rpm and 25 mV/s in 1 M KOH

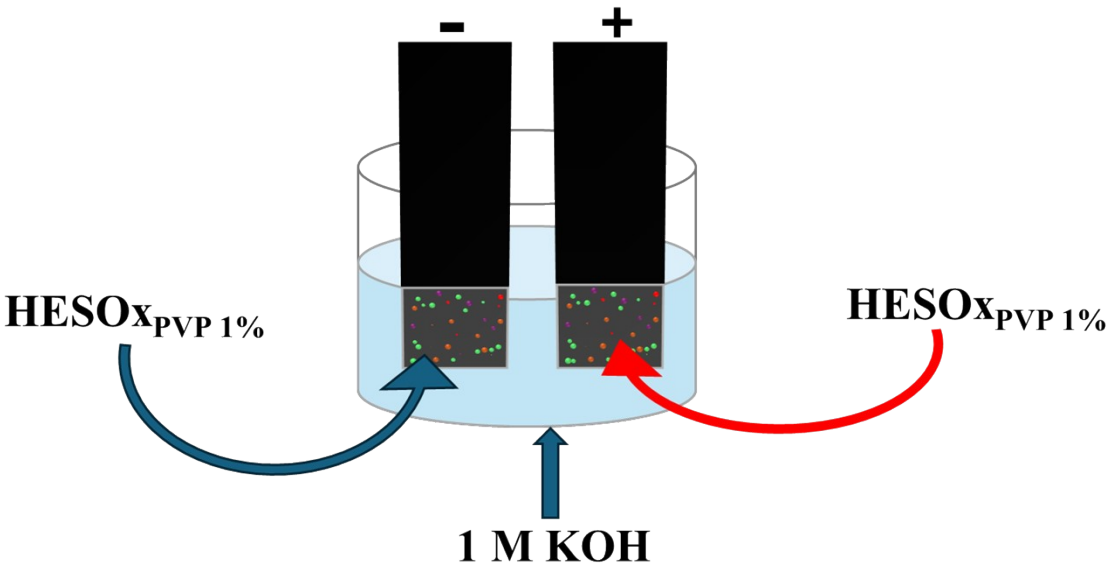

Scheme S 5: A schematic representation of the two-electrode water-splitting setup

Table S 1: Specific surface area and porosity analysis of the samples using the GSA method

Electrocatalysts	Pore size (nm)	Pore volume (cm^3/g)	SSA (m^2/g)
HESOx	15.9931	0.0121	3.0157
HESOx-PVP	10.1300	0.0230	9.0919
HESOx-SDS	17.5393	0.0702	16.0064
HEOx-CTAB	14.3085	0.0439	12.2809

Table S 2A: XPS O 1s binding energies

	O 1s							
	HESOx		**HESOx-PVP**		**HESOx-SDS**		**HESOx-CTAB**	
	Peak center (eV)	**Area**	**Peak center (eV)**	**Area**	**Peak center (eV)**	**Area**	**Peak center (eV)**	**Area**
O 1s lattice oxygen (O_L)	529.6451	14732.8044	529.5874	14775.4178	529.7901	15725.5764	529.6850	10123.6323
O 1s C-O oxygen vacancy (O_V)	531.7126	14767.6819	531.6430	8241.1237	531.6752	12412.5769	531.7146	6906.6365
O 1s C=O (adsorbed species, O_{ads})	533.1553	12298.1541	533.1815	5440.2682	533.2459	8321.6609	533.2027	5761.0774
O_V/O_L	1.00		0.56		0.79		0.68	
O_V/O_{ads}	1.20		1.51		1.49		1.19	
Overall surface contamination (%)	29.42		19.12		22.82		25.28	

Overall surface contamination (%) = $O_{ads}/(O_V + O_L + O_{ads})$

Table S 2B: XPS binding energies

Sample / Chemical species	Binding Energies (eV)/Peak Area (CPSeV)												
	HESOx				HESOx-PVP				HESOx-SDS				
	$2p_{3/2}$	Area	$2p_{1/2}$	Area	$2p_{3/2}$	Area	$2p_{1/2}$	Area	$2p_{3/2}$	Area	$2p_{1/2}$	Area	$2p_{3/}$
Cu^0	932.70	2580.67	952.84	2373.57	932.42	4047.91	952.382	2467.33	933.06	5338.64	953.05	3869.92	932.7
Cu^{2+} (CuO)	933.71	5924.32	953.96	2264.24	933.43	10511.02	953.441	4665.29	934.14	7428.09	954.61	5030.53	933.7
Cu^{2+} ($Cu(OH)_2$)	935.04	9915.99	955.27	2408.53	934.74	15004.58	954.842	6508.19	935.33	7958.30	956.68	1215.82	934.8
Ni^{2+}	855.37	5876.04	873.68	3876.19	854.28	2743.54	871.557	480.13	855.40	16235.75	874.24	9343.55	855.5
Ni^{3+}	857.78	8637.42			855.95	3440.53	873.255	2163.35	857.62	23445.55			857.3
Co^{2+}	780.83	13622.79	797.09	7902.61	780.07	4368.39	795.740	1974.64	780.58	17235.84	797.46	3724.46	781.2
Co^{3+}	783.75	32496.69			782.52	2611.52			782.91	35950.00			784.2
Fe^{2+}	709.49	2493.77	723.19	2690.27	709.49	2165.73	723.102	2603.43	709.59	3040.33	723.87	4401.69	709.8
Fe^{3+}	710.59	6482.57	724.89	4029.63	710.81	4330.78	725.202	1244.77	710.81	6082.76	725.86	405.22	711.2
Mn^0					638.21	20631.63			637.40	1882.57			
Mn^{2+}	640.29	23145.90	649.53	48224.66	641.28	59601.16	648.767	87613.87	640.70	1468.59	648.72	2596.28	640.6
Mn^{3+}	642.74	36294.02	654.60	26607.00	643.74	41097.92	654.650	19026.85	642.11	5025.51	652.09	2207.09	642.6

Table S 3: A summary of the C_{dl} and ECSA of the electrocatalysts

Electrocatalyst	C_{dl} (mF/cm^2)	ECSA (cm^2)
HESOx	6.75	33.075
HESOx-PVP	7.33	35.917
HESOx-SDS	6.95	34.055
HESOx-CTAB	5.63	27.587

Table S 4: A summary of the electrochemical performances of the electrocatalysts

Sample	**HER E @ 10 mA/cm^2 (mV)**	**HER E @ 30 mA/cm^2 (mV)**	**HER E @ 200 mA/cm^2 (mV)**	**OER η @ 10 mA/cm^2 (mV)**
HESOx	-117	-306.9	-642.3	419
HESOx-PVP	**-87**	-305.3	-657.8	**415.8**
HESOx-SDS	-267	-363	-679.6	490.3
HESOx-CTAB	-311	-418	-920	463.7
10 wt % Pt/C	-18	-85.7	-569.1	
IrO_2				507.2

Table S 5: Gas Sorption Analysis

Sample	Pore size (nm)	Pore volume (cm^3/g)	SSA (m^2/g)
$HESOx_{PVP\ 0.5\%}$	10.13	0.023025	9.0919
$HESOx_{PVP\ 1\%}$	11.3591	0.06193	21.8080
$HESOx_{PVP\ 3\%}$	15.3963	0.03723	9.6725
$HESOx_{PVP\ 5\%}$	15.2098	0.01015	2.6682
$HESOx_{PVP\ 10\%}$	14.6691	0.00583	1.5909
$HESOx_{PVP\ 20\%}$	15.9401	0.01142	2.8653
$HESOx_{PVP\ 50\%}$	18.6815	0.04467	9.5642

Table S 6: A summary of the C_{dl} and ECSA of the electrocatalysts

Electrocatalyst	C_{dl} (mF/cm^2)	ECSA (cm^2)
$HESOx_{PVP\ 0.5\%}$	7.33	35.917
$HESOx_{PVP\ 1\%}$	8.68	42.533
$HESOx_{PVP\ 3\%}$	5.71	27.98
$HESOx_{PVP\ 5\%}$	5.75	28.175
$HESOx_{PVP\ 10\%}$	7.63	37.388
$HESOx_{PVP\ 20\%}$	7.04	34.495
$HESOx_{PVP\ 50\%}$	7.82	38.318

Table S 7: A summary of the electrochemical performances of the electrocatalysts

Sample	HER E @ 10 mA/cm² (mV)	HER E @ 30 mA/cm² (mV)	HER E @ 200 mA/cm² (mV)	OER η @ 10 mA/cm² (mV)
$HESOx_{PVP\ 0.5\%}$	-87	-305.3	-657.8	415.8
$HESOx_{PVP\ 1\%}$	-16	-325.6	-653.8	381
$HESOx_{PVP\ 3\%}$	-84	-306.5	-662.4	413
$HESOx_{PVP\ 5\%}$	-117	-297.2	-684.3	423
$HESOx_{PVP\ 10\%}$	-167	-303.7	-684.9	442.6
$HESOx_{PVP\ 20\%}$	-141	-311.5	-673.3	419.8
$HESOx_{PVP\ 50\%}$	-284	-387.3	-779.9	421.1

Table S 8: EIS Analysis

	HER		
Sample	R_s (Ω)	R_{diff} (Ω)	R_{ct} (Ω)
$HESOx_{PVP\ 0.5\%}$	6.2	7.6	935.6
$HESOx_{PVP\ 1\%}$	6.1	0.8	749.8
$HESOx_{PVP\ 3\%}$	5.9	0.9	1343
$HESOx_{PVP\ 5\%}$	6.9	3.2	1327
$HESOx_{PVP\ 10\%}$	6.1	5.7	1129
$HESOx_{PVP\ 20\%}$	2.8	2.8	1021
$HESOx_{PVP\ 50\%}$	6.1	4.7	1475

Table S 9: A comparison of the two-electrode water splitting performance with Pt/C||IrO_2 mix and literature in 1 M KOH

Sample	**E @ 10 mA/cm^2 (V)**	**Ref**
$HESOx_{PVP\ 1\%}$	1.497	**This work**
Pt/C||IrO_2	1.74	**This work**
NiFe-LDH/Ni/$NiCo_2S_4$/NF	1.53	[2]
HEO–MoS_2	1.65	[3]
Ru-$NiSe_2$/CoSe/NF-4	1.53	[4]
AlNiCoRuMo	1.50	[5]
CoFe-LDH-MoO_4^{2-}	1.50	[6]
$CuCo_2S_{3.68}Se_{0.32}$	1.52	[7]
CoPc/SWCNT	1.655	[8]
Cu_3P/g-C_3N_4	1.54	[9]
RuCu/C-3	1.54	[10]

References

1 C. Tsioptsias, *Measurement*, 2022, **204**, 112136.

2 X.-S. Gong, X. Liu and J. Zhou, *Nanoscale*, 2025, **17**, 5301–5315.

3 S. C. Pathan, J. S. Shaikh, N. S. Shaikh, V. Márquez, M. Rittiruam, T. Saelee, P. Khajondetchairit, S. S. Mali, J. V Patil, C. K. Hong, P. Praserthdam and S. Praserthdam, *S Afr J Chem Eng*, 2024, **48**, 425–435.

4 Y. Wang, J. Xiao, T. Huang, Y. Wang, H. Ding, Q. Zhu, G. Xu and L. Zhang, *Nanoscale*, 2025, **17**, 14278–14289.

5 Z. Jin, J. Lyu, Y. Zhao, H. Li, X. Lin, G. Xie, X. Liu, J.-J. Kai and H.-J. Qiu, *ACS Materials Lett.*, 2020, **2**, 1698–1706.

6 Z. Guo, Y. He, P. Chen, R. Li, Z. Wang, X. Xu, S. Chang, Y. Li, R. Jia and S. Han, *Int J Hydrogen Energy*, 2024, **92**, 1500-1507.

7 B. Zhang, X. Qian, H. Xu, L. Jiang, J. Xia, H. Chen and G. He, *Nanoscale*, 2023, **15**, 16199–16208.

8 Q. Mo, Y. Meng, L. Qin, C. Shi, H.-B. Zhang, X. Yu, J. Rong, P.-X. Hou, C. Liu, H.-M. Cheng and J.-C. Li, *ACS Appl Mater Interfaces*, 2024, **16**, 16164–16174.

9 Sk. Riyajuddin, T. Aziz, S. Kumar, G. D. Nessim and K. Ghosh, *ChemCatChem*, 2020, **12**, 1394–1402.

10 D. Pan, Q. Liu, B. Yu, D. B. DuBois, J. Tressel, S. Yu, N. Kaleekal, S. Trabanino, Y. Jeon, F. Bridges and S. Chen, *Small*, 2024, **20**, 46, 2404729.